ELSEVIER

Contents lists available at ScienceDirect

International Journal of Solids and Structures

journal homepage: www.elsevier.com/locate/ijsolstr





Adherence of a hyperelastic shell on a rigid planar substrate

Chenxu Zhao^a, Xuanhan Chen^a, Wanliang Shan^{a,*}, Kai-tak Wan^{b,*}

- ^a Mechanical Engineering, Syracuse University, NY, United States
- b Mechanical & Industrial Engineering, Northeastern University, MA, United States

ARTICLE INFO

Keywords: Adhesion Hyperelasticity Shell

ABSTRACT

A hyperelastic shell with spherical cap geometry is compressed to a rigid planar substrate. Using Maugis' graphical method and a numerical approach, the quasi-static adhesion-detachment trajectory, the interrelation between applied load, approach distance and contact radius, and the critical pull-off parameters are determined for ranges of materials stiffness, shell thickness, shell depth and interfacial adhesion energy.

1. Introduction

Adhesion is ubiquitous in a wide spectrum of manmade and natural systems, for instances, robotic grippers (Swift et al., 2020; Mohammadi Nasab et al., 2020; Tatari et al., 2018; Carlson et al., 2012; Croll et al., 2019), stiction in nano-/micro-electromechanical systems (N/MEMS) and nano-structures (Grierson et al., 2005; Joulaei et al., 2020; Wong et al., 2007), biomedical devices such as drug-eluting stents (Meng et al., 2010; Du et al., 2012), bio-inspired adhesives for robotic locomotion (Kern et al., 2017; Sharifi et al., 2021), bacterial strains adhering on filters (Sun et al., 2020; Shi et al., 2013; Shi et al., 2012; Shi et al., 2011), and contact lenses (Wang et al., 2018). Despite the voluminous literature in thin film and high post adhesion/delamination (e.g. Luo et al., 2020; Freund and Suresh, 2009), adhesion mechanics of shells is comparatively rare due to geometrical incompatibility and involved mathematical formulation (Hutchinson, 2016).

The Johnson-Kendall-Roberts (JKR) theory has been the standard model for solid-solid adhesion and meets many successes for decades (Johnson et al., 1971; Ciavarella et al., 2019). Modifications and reexamination of the basic model have been extended to include surfaces with corrugation, undulation and roughness (Kern et al., 2017; Guduru and Bull, 2007; Davis and Crosby, 2011), long-range intersurface attractions (Grierson et al., 2005) etc. for a range of materials using analytical and computational techniques (Sauer, 2016). In this paper, we focus on adhesion of shells prone to deformation and conformation to substrate topology which is essential in designing robotic grippers, for instance. Although mechanics of thin shells has been investigated for decades especially for elastic materials, small deformation and buckling (Timoshenko and Woinowsky-Krieger, 1959; Flügge, 1973; Reddy,

2007; Hutchinson, 2020), and adhesion of cylinders (Shi et al., 2013; Shi et al., 2012; Majidi and Wan, 2010; Tang et al., 2005).

The JKR model is constructed based on the classical Hertz theory where two elastic spheres come into intimate adhesion contact (Johnson et al., 1971; Maugis, 2000). External compression results in elastic deformation and a small planar interface due to geometrical incompatibility. In case of shells, a relatively small compression results in large contact area conforming to the substrate geometry. Shell thickness plays a crucial role in the adhesion mechanics. Our earlier spherical shell adhesion model is limited to linear elastic materials and small contact radius compared to shell radius (Shi et al., 2011). In this paper, we attempt to construct a model for large deformation in a hyperelastic shell. Rather than a convoluted analytical model which is difficult to apply to real situations, we will resort to a numerical approach for shells with specific dimension. We will adopt Maugis' graphical method (Maugis, 2000) to investigate the behavior of a thin shell of finite thickness under large deformation. The shell taking the shape of a spherical cap is pressed against a rigid planar substrate in the presence of a strong intersurface attractive force with negligible range. The shell is deformed by a combined applied load and adhesion and is then allowed to relax while the contact area remains constant. The adhesiondetachment behavior and trajectory is numerically determined by minimization of the total energy comprising the potential energy due to the external load, the elastic energy stored in the shell, and the surface energy due to expanding or shrinking of the contact area. Unlike the classical Hertz contact, the elastic energy is derived from a nonlinear constitutive relation. We will demonstrate the working principle for a neo-Hookean solid shell. The interrelation between the measurable quantities of external compressive load, P, approach distance, δ , and

E-mail addresses: washan@syr.edu (W. Shan), ktwwan@coe.neu.edu (K.-t. Wan).

^{*} Corresponding authors.

contact radius, a, will be numerically determined for a range of materials compliance. The critical parameters of (P^*, δ^*, a^*) at pull-off or spontaneous detachment will also be computed.

2. Theory

Fig. 1 shows a hemispherical shell with radius of curvature, R, and thickness, t, pressing against a rigid planar substrate. The shell is made of an incompressible hyperelastic material governed by the neo-Hookean limit of the Mooney-Rivilin model given by the strain energy potential, $U=C_{10}\left(\overline{I}_1-3\right)$, with C_{10} the material parameters, $\overline{I}_1=\overline{\lambda}_1^2+\overline{\lambda}_2^2+\overline{\lambda}_3^2$ the first deviatoric strain invariant, $\overline{\lambda}_i=J^{-\frac{1}{3}}\lambda_i$ the deviatoric

stretches, *J* the total volume ratio, and λ_i the principal stretches.

An external load is applied at the rim of the base with fixed radius, b. Similar to JKR, the constitutive relation is first established in the absence of adhesion with $\gamma = 0$. The mechanical response $P(\delta)$ is found using the finite element analysis software ABAQUS. Details of the mesh is given in Appendix. Initial loading with $\delta \ll t$ leads to a small contact area where the compressive stress field in the shell is confined. The mechanical response $P(\delta)$ is in essence uninfluenced by t or R, and approaches the Hertz limit. As δ reaches or exceeds t, a becomes comparable with R, resulting in large strain close to the contact and large global geometrical deformation. The stress field grows beyond the contact region and extends quickly to the entire thin shell. The global deformation leads to a bending dominant stress in both meridional and azimuthal directions. Fig. 2 shows the deformed profile and the von Mises stresses at excessive loading under compression and tension. In the absence of interfacial adhesion ($\gamma = 0$), compression (P > 0) leads to bulging at a ring below the rim where the diameter exceeds the rim dimension, a distinct feature of shells absent in solid spheres, as shown in Fig. 3. Stress field is axisymmetric about the shell axis and reaches a maximum close to the contact edge where maximum deformation is present. Within the contact circle, stress is a maximum at the contact interface, but vanishes close to the center. When the shell is sufficiently compressed, a large differential stress can cause buckling. At the contact edge, the shell surface form a sharp cusp in reminiscence of the Hertz contact. Now, say, a specific adhesion is introduced at the shell-substrate interface that maintains a independent of P and δ . A tensile load (P < 0) deforms the shell geometry. The contact edge turns into the classical Griffith-JKR parabola, contrasting the Hertzian cusp (Maugis, 2000). The contact circle now resembles a crack front in mode I fracture in an elastic solid, and its stress becomes singular where a non-zero stress intensity factor can be defined.

Fig. 4 shows the mechanical response, $P(\delta)$. In the absence of adhesion, an external compressive load of $P_1 = P + P_{ad}$ is first applied to give rise to a deformed geometry with δ_1 and a. Contrasting the Hertz contact theory for an elastic sphere with $P \propto \delta^{3/2}$, a significant deviation occurs in $P(\delta)$ for a hyperelastic shell with bulging close to the base rim where external loading is acting. To account for a zero-range intersurface attractive force or adhesion ($\gamma > 0$) at the shell-substrate interface, the

circular contact area is in intimate contact with the substrate and a is forced to remain constant hereafter. The external load now reduces from P_1 to P_1 and the approach distance from P_1 to P_2 following a path of P_2 following a path of P_2 following a path of P_2 following a path of the strictly linear. Here P_2 following a path of the shell is thus given by

$$U_E = \int_0^{\delta_1} P \cdot d\delta - \int_{\delta}^{\delta_1} P_{rel} \cdot d\delta \bigg|_{C} \tag{1}$$

The first integral corresponds to initial loading from P=0 to P_1 and $\delta=0$ to δ_1 with a varying a. The second integral is the energy recovered from relaxation from P_1 to P and δ_1 to δ with a constant a. The total energy U_T of the system can now be written as

$$U_T = U_P + U_E + U_S \tag{2}$$

where $U_P = -P \cdot \delta$ is the potential energy of the applied load and $dU_P = P \cdot d\delta$, and $U_S = -A \cdot \gamma$ is the surface energy to expand the contact area $A = \pi a^2$ and $dU_S = -2\pi a \cdot \gamma \cdot da$. Thus, U_T is determined as a function of A. The strain energy release rate is defined as $G = d(U_P + U_E)/dA$. There are two possible loading configurations. Under a fixed load (P =constant) or the shell being loaded by a dead weight, $U_T(A)$ is defined for specific values of P. Minimization of U_T , or, $dU_T/dA = 0$, yields the quasi-static thermodynamic balance with $G = \gamma$. Stable equilibrium further requires a local minimum in $U_T(A)$, or, $d^2U_T/dA^2 > 0$ or dG/dA > 0. As load turns more negative (tension), the local minimum turns into a point of inflexion with $d^2U_T/dA^2 = 0$, "pull-off" occurs when the contact circle spontaneously vanishes, and the shell detaches from the substrate. Under a fixed-grips configuration ($d\delta = 0$), $U_T(A)$ is defined for specific value of δ . Here $dU_P = -P \cdot d\delta = 0$ and $U_T = U_E + U_S$. Though equilibrium occurs also at $G = \gamma$ similar to the fixed-load counterpart, the nature of stability is quite different. We will demonstrate the equilibrium conditions and stability using a graphical method outlined below.

Fig. 4 shows schematic $P(\delta)$ under loading and relaxation. Fig. 4a shows P>0 and $\delta>0$. In the absence of adhesion ($\gamma=0$), initial loading to P_1 follows OA. Elastic energy stored in the elastic shell is given by Area(OAC'O). Relaxation to P proceeds along AB such that an energy of Area(AC'CBA) is recovered. The net elastic energy is thus U_E = Area (OABCO) = Area(OAC"O) + Area(C"BCC"). Potential energy loss due to the applied load is U_P = -Area(OB"BCO). Therefore, U_T = Area (-OB"BCO + OABCO) $-\pi a^2 \gamma$. Fig. 4b shows P<0 and $\delta>0$ with U_E = Area(OABCO) = Area(OAC"O) + Area(C"BCC") and U_P = Area (OCBB"O). Fig. 4c shows P<0 and $\delta<0$ with U_E = Area (OABCO) = Area(OAC"O) + Area(C"BCC") and U_P = -Area (OABCO) = Area(OAC"O) + Area(C"BCC") and U_P = -Area (OB"BCO). Minimization of U_T thus allows the adhesion-detachment mechanics to be determined for a constant γ .

3. Results

The graphical-numerical scheme is applied to the nonlinear shell deformation. We will first trace the adhesion-detachment trajectory before delving into the effects due to changing shell materials and

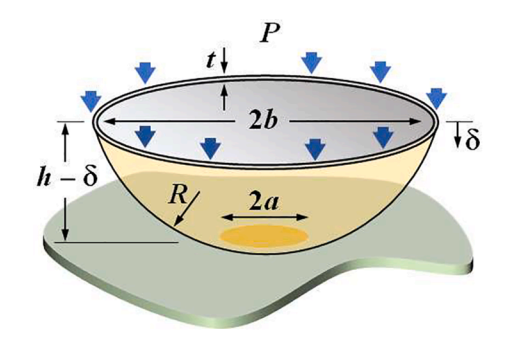




Fig. 1. Schematic of a shell under an external vertical load at the rim pressing against a rigid planar substrate.

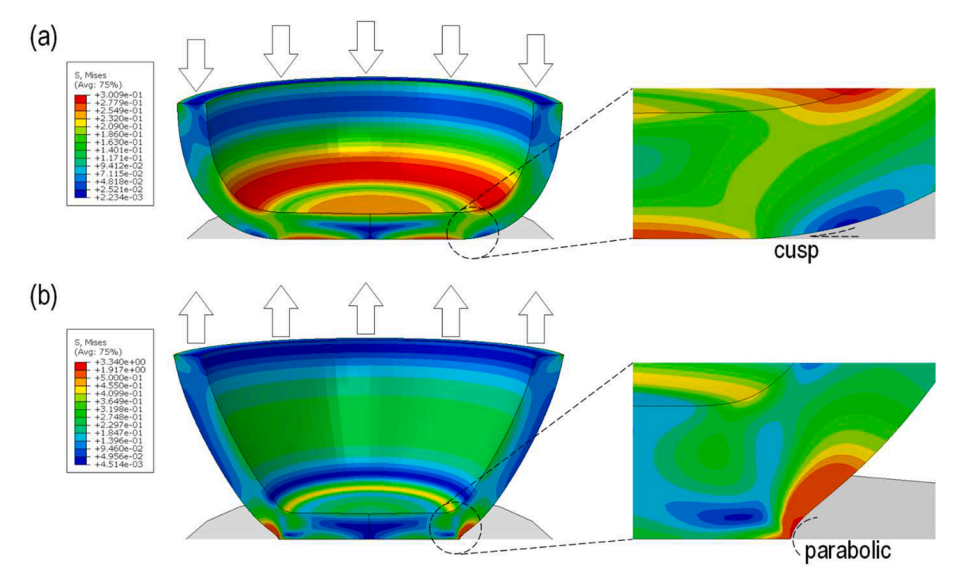


Fig. 2. Deformed geometry and von Mises stress of a shell with R=h=20 mm and t=3 mm. (a) A shell under compressive load (P=14.67 N, $\delta=5$ mm, a=10 mm) in the absence of interfacial adhesion ($\gamma=0$). A magnified contact edge is shown on the right, showing a cusp geometry. (b) A shell under tensile load (P=-35.49 N, $\delta=0$ mm, a=10 mm). The contact circle is a constant and does not vary with external load. The contact edge shows the classical Griffith-JKR parabola. Within the contact circle, stress is close to zero around the shell axis though the top and bottom surface are under large stress. In an extreme condition, the shell buckles inwards turning into a dome and detaching from the substrate.

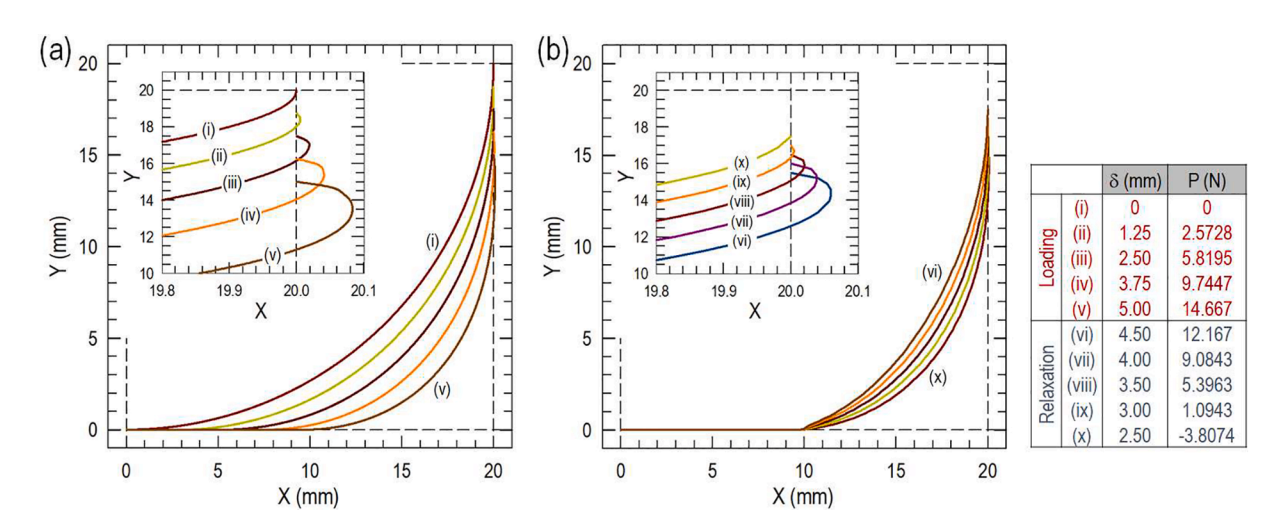


Fig. 3. Typical deformed profiles of a shell with R = h = 20 mm, t = 3 mm and $C_{10} = 0.30$ MPa. (a) Loading under increasing compression with P > 0 and a changing contact radius a to maintain equilibrium. (b) Unloading with external load turning from compressive (P > 0) to tensile (P < 0) and contact radius maintained at a = 10 mm. Bulging occurs below the rim when P > 0 as in curves (i)-(ix), but disappears when P vanishes and turns negative as in curve (x).

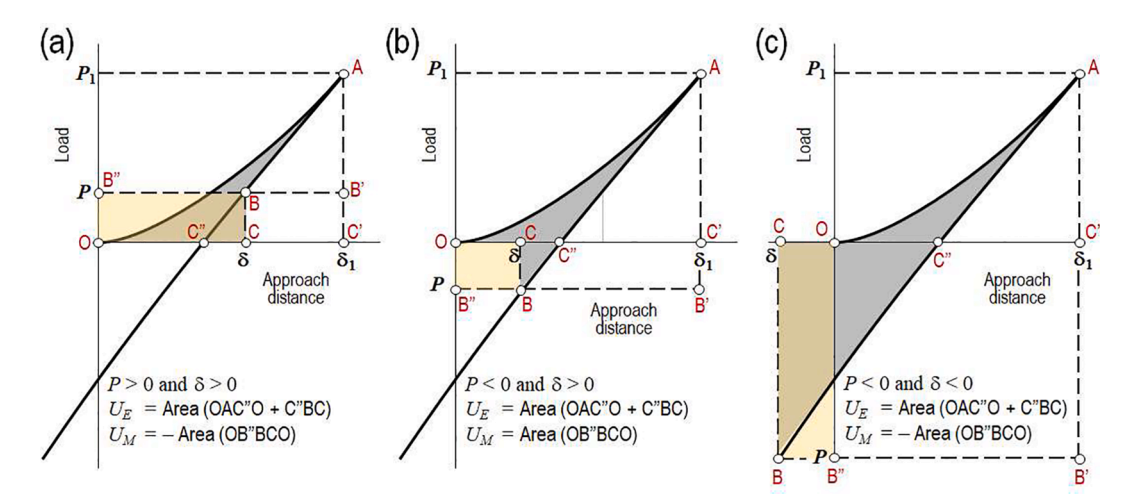


Fig. 4. Ideal mechanical response of loading (compression) to unloading (tension) of a hyperelastic hemispherical shell: (a) External compression: both *P* and δ are positive, (b) External compression: *P* is positive while δ is negative, (c) External tension: both *P* and δ are negative. Shaded areas represent energy involved.

geometry as well as interfacial properties.

3.1. Adhesion-detachment trajectory

Fig. 5 shows the detachment trajectories of fixed-load and fixed-grips for a constant γ . Under a *fixed-load*, U_T is found numerically as a function of A such that a family of $U_T(A)$ curves can be generated for a range of fixed P. All curves with $P < P^*$ possess a local minimum corresponding to a stable equilibrium with $G = \gamma$. The contact circle shrinks along path ABCDE as P turns gradually from compressive (P > 0) to tensile (P < 0). At E, $P = P^*$ and the local minimum turns into an inflexion. Small disturbance forces the contact circle to shrink spontaneously to zero to minimize U_T , and the shell detaches from the substrate at pull-off. The critical parameters (P^* , δ *, a^*) are determined numerically. Under *fixed-grips*, detachment proceeds along ABCDE passing the minima of $U_T(A)$ with fixed δ . The interrelation of (P, δ , a) is identical to that of fixed-load equilibrium but not in terms of stability. Loading remains stable at (P^* , δ *, a^*) and continues further to (P^{\dagger} , δ †, a^{\dagger}) at E where pull-off occurs under fixed-grips.

3.2. Varying geometry and materials properties

Fig. 6a shows shrinkage of the contact circle as the external tensile load increases for ranges of materials stiffness (C_{10}), shell thickness (t/R), shell depth (h/R) and adhesion strength (γ). Pull-off under fixed load

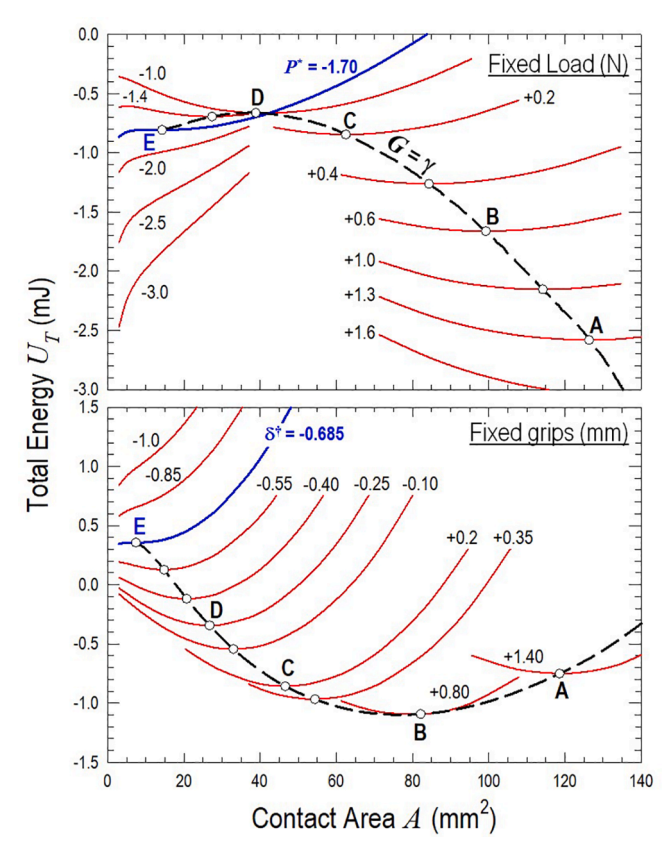


Fig. 5. Energetics of a shell with R=h=20 mm, t=3 mm, $C_{10}=0.30$ MPa and $\gamma=30$ J m $^{-2}$. Above: Total energy of systems as a function of contact area under *fixed-load* conditions. Each curve corresponds to a specific load P as indicated, and the minima are marked by O. The dashed curve ABCDE shows the locus of stable equilibrium $(G=\gamma)$. At $P^*=-1.70$ N (tension), $\delta^*=-0.563$ mm, and $a^*=2.13$ mm, $U_T(A)$ possesses only one inflexion at E where pull-off occurs. Below: $U_T(A)$ under *fixed-grips* with constant δ indicated on each curve. The dashed curve is the locus of stable equilibrium similar to fixed-load in (a). At $\delta^\dagger=-0.685$ mm, $P^\dagger=-1.640$ N (tension), and $a^\dagger=1.598$ mm, "pull-off' occurs.

at P^* occurs when dP/da = 0 or $da/dP \rightarrow \infty$. Fig. 6b shows P^* as a function of the listed variables.

- (i) Varying materials stiffness. Compared to stiff shells, a compliant shell with small C_{10} under the same compressive load deforms more significantly in terms of a and δ . Increasing C_{10} in the range considered leads to larger P^* . Contrasting JKR, here P^* depends on the mechanical properties of the shell.
- (ii) Varying shell thickness. In case of a solid hemisphere with t=R, the JKR limit of $P^*=(3/2)\,\pi\,R\,\gamma$ is expected. The same behavior is expected in a very thick shell with t=0.5R as shown, since deformation and stress remain localized at the contact area. Transition from thick to thin shell is demonstrated for $t=4.5\,$ mm = 0.225R. Pull-off occurs at P^* significantly lower than JKR, and $a^*\approx 2.265\,$ mm is comparable with t, implying that the stress field is no longer confined but spreads extensively to volume beyond the contact area. As t reduces to 0.175 R, P^* diminishes further and a(P) significantly deviates from JKR.
- (iii) Varying shell depth. Deep shells with $h \approx R$ have similar behavior. The shell appears stiff due to the inevitable bulging at large P. Shallow shells with h < 0.75R are compliant. P^* falls in roughly the same range rather independent of h.
- (iv) *Varying adhesion*. Increasing adhesion shifts $P^*(\gamma)$ to a higher $|P^*|$ and a(P=0). The linear relation of $P(\gamma)$ from our results has a slope of $dP^*/d\gamma \approx 0.050$ m. JKR also predicts a linear $P(\gamma)$ with a slope of $(dP^*/d\gamma)_{\rm JKR} = (3/2) \pi R \approx 0.094$ m for R=20 mm, comparable to that of a shell.

Note that these trends are valid only in the specified ranges as indicated. Once the basic assumptions break down as in case of buckling of the contact area, modification is necessary to accommodate other deformation mode and adhesion-detachment trajectory.

4. Discussion

The numerical routine to determine adhesion-detachment of a shell is demonstrated. A few other shell characteristics are not addressed. For instance, one major assumption is the conformation of shell to the substrate topology and the contact circle remains planar and in intimate contact. A very large deformation of a thin shell leads to inward buckling of the contact area in order to minimize the stored elastic energy. In fact, Fig. 2 shows an intense von Mises stress at the contact interface, but the stress reduces to virtually zero close to the contact area center. As the difference in stresses on the top and bottom surface of the shell increases upon external loading, buckling occurs and the central plate detaches from the substrate while the contact edge remains in intimate contact. In case of strong adhesion, the contact area remains planar. However, if adhesion is too weak to reinforce contact planarity, buckling becomes inevitable and the contact becomes a ring with an area $\pi(a_{out}^2 - a_{in}^2)$ with and outer and inner radii, a_{out} and a_{in} , respectively. Minimization of U_T remains valid to determine equilibrium, but the new intriguing geometry posts extensive revision of the adhesion-detachment trajectory compared to the present work.

It is worthwhile to compare the present model with our previous work in shell adhesion (Shi et al., 2011). The earlier model is based on a linear elastic hemispherical shell which is relatively stiff, and the shell is thus under bending dominant deformation. The planar contact circle is therefore small compared to the radius of curvature and approach distance. The stress is in essence confined to the small contact area and the vicinity. Thermodynamic energy balance yields a pull-off force of

$$P^* = \eta \left[\frac{\gamma^4 R^4 (1 - v^2)}{E t^2} \right]^{1/3} \tag{3}$$

with *E* and *v* the elastic modulus and Poisson's ratio of the shell material and $\eta = 13.2 \pm 0.6$ from curve-fitting. It is therefore expected that

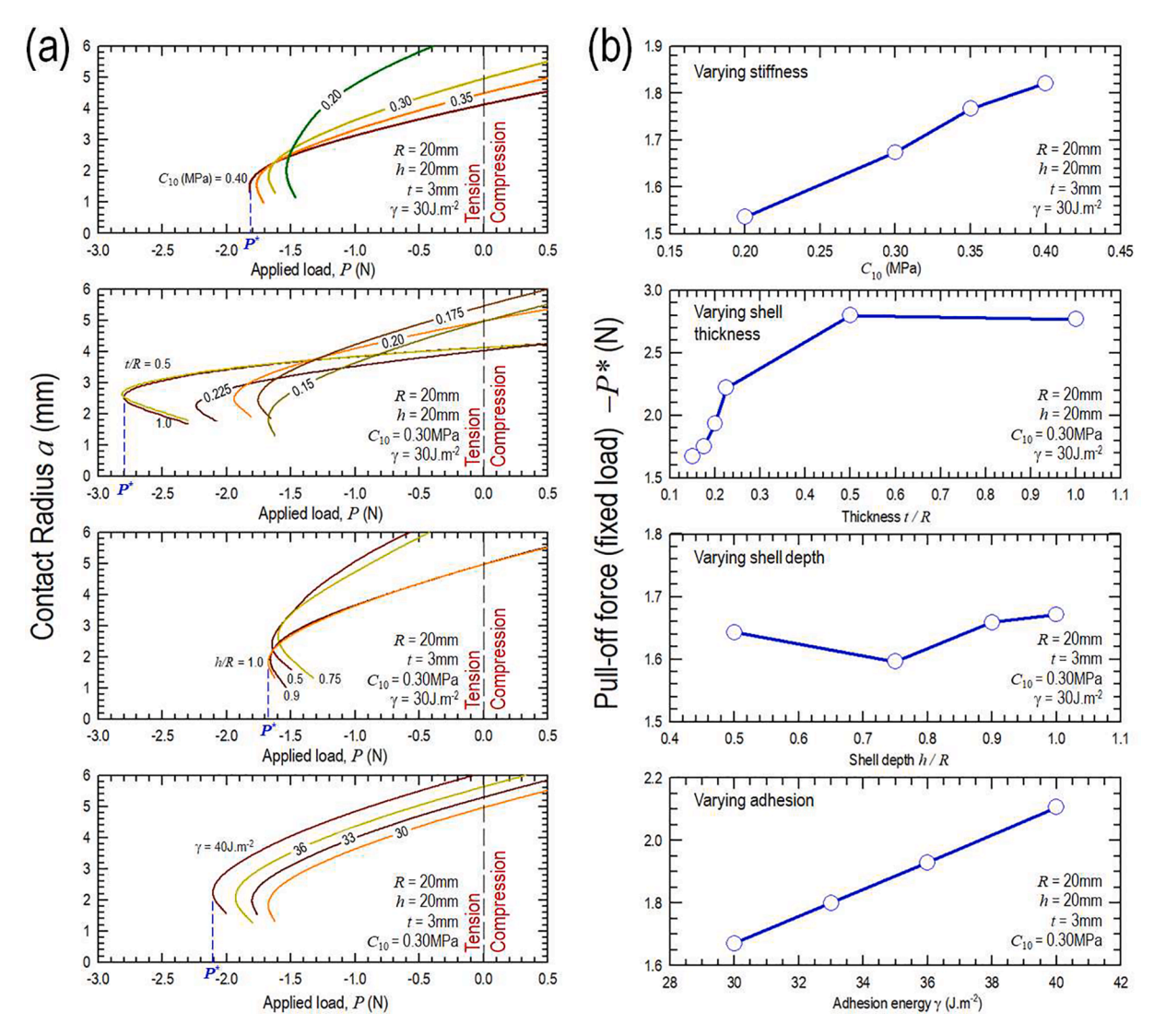


Fig. 6. (a) Contact area as a function of external load for ranges of shell materials stiffness, shell thickness, shell depth, and adhesion energy. "Pull-off" occurs at *P** when the external load reaches the maximum tension. (b) Pull-off force under fixed load obtained from part (a).

 $P^*\propto \gamma^{4/3}$, $P^*\propto E^{-1/3}$, and $P^*\propto t^{-2/3}$. In terms of materials stiffness and shell thickness, it is remarkable to find the opposite trend of both $P^*(C_{10})$ and $P^*(t)$ being monotonically increasing in the present model (c.f. Fig. 6b), though P^* increases with γ as expected. The nonlinear properties, large deformation, and bulging profile not captured in the earlier model are the main reasons for differences in trends. Nevertheless, based on the numbers shown in Fig. 6, the constant η spans the range of roughly 7 to 11, which is reasonably close to our earlier result.

When a shell is under a very compressive load leading to very large deformation, buckling within the contact circle becomes inevitable to reduce the elastic energy density, especially when the shell-substrate interface is not strong enough to pull the opposing surfaces into intimate contact. Buckling is ignored in the present work. One possible justification is the assumed JKR-limit where the intersurface force has an *infinite* magnitude but *zero* range giving rise to a finite adhesion energy (Maugis, 2000; Wan and Julien, 2009). More sophisticated mathematical treatment is necessary to establish the buckling criteria in the presence of adhesion, for instance, a dimensionless number involving R, h, t, b, δ , γ and C_{10} , which is apparently beyond the scope of this short paper.

A related geometry of interest is the pressurized blister (Zhu et al., 2017; Plaut, 2021). A film detaches from a substrate when the internal gas pressure exceeds the external atmosphere. The delamination

trajectory is tracked by a mechanical energy balance depending on the nature of the thermal process. In case of a fixed applied pressure pushing on the membrane in an isobaric manner, the governing equation can be found in standard fracture mechanics textbook. Alternatively, if the membrane traps a fixed amount of working gas, either heating or exposing the sample to a vacuum causes the gas to expand to drive a delamination. Here the thermal processes can be either isothermal where simple gas law is applicable or isentropic where the gas cools down upon expansion (Wan, 2000; Wan and Breach, 1998). The analytical method can be applied to shell adhesion where pressure can be applied in addition to mechanical compression. Gas can also be trapped in the hemispherical void, while external compressive leads to increase in internal pressure. An energy balance can be derived but is beyond the scope of the present paper.

It is remarkable that the present work has a wide range of potential applications. For instance, in case of robotic grippers, the present work can help to identify the right materials for best performance, to design the optimal shell thickness and radius of curvature, and to assess the device performance in the presence of environmental species such as water and the resulting intersurface forces.

5. Conclusion

We have demonstrated how the adhesion-detachment of a shell from a planar rigid substrate can be derived using a JKR-based graphical-numerical method combined with finite element analysis. Interrelation between applied load, approach distance and contact radius, and its dependence on the shell geometry, materials and intersurface properties, are derived for specific shells. The trends contrast expectations in the literature of JKR-type solid–solid adhesion. The approach is particularly useful when the shell is made of nonlinear materials with several parameters and subject to large deformation where an analytical solution is unlikely achievable.

Declaration of Competing Interest

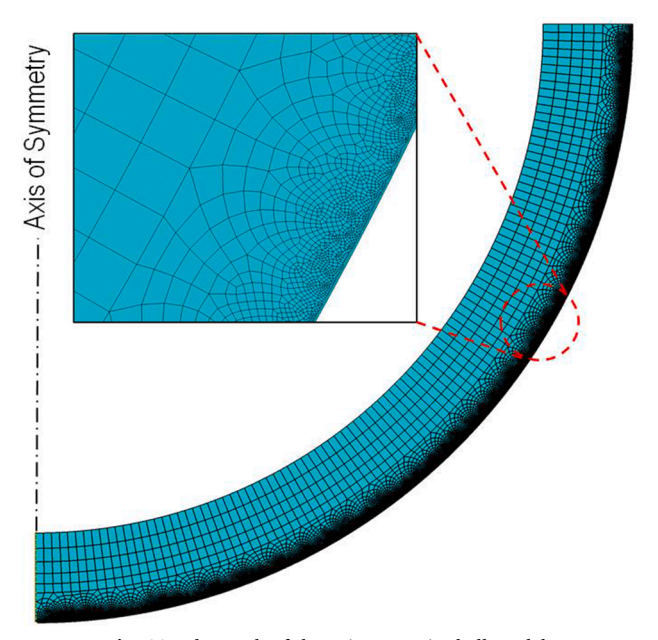
The authors declare that they have no known competing financial interests or personal relationships that could have appeared to influence the work reported in this paper.

Acknowledgements

The authors acknowledge the financial support by Syracuse University through startup fund for Wanliang Shan, and National Science Foundation awards CMMI #2006430 and CBET #1705757. Any opinions, findings, and conclusions or recommendations expressed in this material are those of the authors and do not necessarily reflect the views of NSF.

Appendix: Finite element mesh

A numerical scheme using FEA-ABAQUS is developed based on *Static*, *General* and an Axisymmetric Deformable model with element CAX4RH. Figure A1 shows the FE mesh and the axis of symmetry. The outer convex surface of the shell is uniformly discretized with fine mesh of 0.01mm, while the inner concave surface comprises mesh up to 0.27mm. A *Cohesive Behavior without Damage* criterion is implemented to ensure full contact within the contact circle. The substrate is fixed by *ENCASTRE*.



 $\textbf{Fig. S1.} \ \ \textbf{The mesh of the axisymmetric shell model}.$

References

Carlson, A., Wang, S., Elvikis, P., Ferreira, P.M., Huang, Y., Rogers, J.A., 2012. Active, programmable elastomeric surfaces with tunable adhesion for deterministic assembly by transfer printing. Adv. Funct. Mater. 22 (21), 4476–4484.

M. Ciavarella, J. Joe, A. Papangelo, J.R. Barber, The role of adhesion in contact mechanics. 16[151] 20180738 (2019).

Croll, A.B., Hosseini, N., Bartlett, M.D., 2019. Switchable adhesives for multifunctional interfaces. Adv. Mater. Technol. 4 (8), 1900193.

Davis, C.S., Crosby, A.J., 2011. Mechanics of wrinkled surface adhesion. Soft Matter 7 (11), 5373–5381.

Du, J., Hampp, E., Shan, W., Li, H., Papandreou, G., Maryanoff, C.A., Soboyejo, W.O., 2012. Adhesion between a suspended polymeric film and a metallic substrate: Experiments and models. J. Mater. Res. 27 (14), 1797–1805.

Flügge, W. (Ed.), 1973. Stresses in Shells. Springer Berlin Heidelberg, Berlin, Heidelberg, Freund, L.B., Suresh, S., 2009. Thin Film Materials: Stress, Defect Formation and Surface Evolution. Cambridge University Press.

Grierson, D.S., Flater, E.E., Carpick, R.W., 2005. Accounting for the JKR-DMT transition in adhesion and friction measurements with atomic force microscopy. J. Adhes. Sci. Technol. 19 (3-5), 291–311. Guduru, P.R., Bull, C., 2007. Detachment of a rigid solid from an elastic wavy surface: experiments. J. Mech. Phys. Solids 55 (3), 473–488.

Hutchinson, J.W., 2016. Buckling of spherical shells revisited. Proc. R. Soc A 472 (2195), 20160577.

Hutchinson, J.W., 2020. EML Webinar overview: New developments in shell stability. Extreme Mech. Lett. 39, 100805.

Johnson, K.L., Kendall, K., Roberts, A.D., 1971. Surface energy and the contact of elastic solids. Proc. R. Soc. Lond. A 324, 301–313.

Joulaei, M., Kolahdoozan, M., Salehi, M., Zadsar, M., Vahabi, M., 2020. Comparison of the adhesion forces in single and double-layer coatings on the MEMS surfaces by JKR and DMT models. Surf. Interface Anal. 52 (1-2), 34-41.

Kern, M.D., Qi, Y., Long, R., Rentschler, M.E., 2017. Characterizing adhesion between a micropatterned surface and a soft synthetic tissue. Langmuir 33 (4), 854–864.

Luo, A., Mohammadi Nasab, A., Tatari, M., Chen, S., Shan, W., Turner, K.T., 2020. Adhesion of flat-ended pillars with non-circular contacts. Soft Matter 16 (41), 9534–9542

C. Majidi, K.-T. Wan, Adhesion between Thin Cylindrical Shells with Parallel Axes. J. Appl. Mech. 77[5] 041013, DOI: 10.1115/1.4000924 (2010).

Maugis, D., 2000. Contact, Adhesion and Rupture of Elastic Solids. Springer, New York.

- Meng, J., Orana, A., Tan, T., Wolf, K., Rahbar, N., Li, H., Papandreou, G., Maryanoff, C., Soboyejo, W., 2010. Adhesion and interfacial fracture in drug-eluting stents. J. Mater. Res. 25 (4), 641–647.
- Mohammadi Nasab, A., Luo, A., Sharifi, S., Turner, K.T., Shan, W., 2020. Switchable adhesion via subsurface pressure modulation. ACS Appl. Mater. Interfaces 12 (24), 27717–27725.
- Plaut, R.H., 2021. Effect of pressure on pull-off of flat cylindrical punch adhered to circular membrane. J. Adhes. (in press) 1–23.
- Reddy, J.N., 2007. Theory and analysis of elastic plates and shells. CRC Press, Taylor and Francis.
- Sauer, R.A., 2016. A survey of computational models for adhesion. J. Adhesion 92 (2), 81–120
- S. Sharifi, C. Rux, N. Sparling, G. Wan, A. Mohammadi Nasab, A. Siddaiah, P. Menezes, T. Zhang, W. Shan, Dynamically Tunable Friction via Subsurface Stiffness Modulation. 8[1911 (2021).
- J. Shi, S. Müftü, K.-T. Wan, Adhesion of a Compliant Cylindrical Shell onto a Rigid Substrate. J. Appl. Mech. 79[7] 041015, DOI:10.1115/1.4005555 (2012).
- J. Shi, S. Müftü, A.Z. Gu, K.-T. Wan, Adhesion of a Cylindrical Shell in the Presence of DLVO Surface Potential. J. Appl. Mech. 80[6] 061007, doi:10.1115/1.4023960 (2013)
- Shi, J., Müftü, S., Wan, K.-T., 2011. Adhesion of an elastic convex shell onto a rigid plate.
 J. Adhes. 87 (6), 579–594. https://doi.org/10.1080/00218464.2011.583587.
- Sun, J., Ran, R., Muftu, S., Gu, A.Z., Wan, K.-T., 2020. The mechanistic aspects of microbial transport in porous media. Colloids Surf., A 603, 125169.

- Swift, M.D., Haverkamp, C.B., Stabile, C.J., Hwang, D., Plaut, R.H., Turner, K.T., Dillard, D.A., Bartlett, M.D., 2020. Active membranes on rigidity tunable foundations for programmable, rapidly switchable adhesion. Adv. Mater. Technol. 5 (11), 2000676.
- Tang, T., Jagota, A., Hui, C.-Y., 2005. Adhesion between single-walled carbon nanotubes.
 J. Appl. Phys. 97 (7), 074304. https://doi.org/10.1063/1.1871358.
- Tatari, M., Mohammadi Nasab, A., Turner, K.T., Shan, W., 2018. Dynamically tunable dry adhesion via subsurface stiffness modulation. Adv. Mater. Interfaces 5 (18), 1800321.
- Timoshenko, S.P., Woinowsky-Krieger, S., 1959. Theory of Plates and Shells, 2nd ed. McGraw-Hill, New York.
- Wan, K.-T., 2000. A novel blister test to investigate thin film delamination at elevated temperature. Int. J. Adhes. Adhes. 20 (2), 141–143.
- Wan, K.-T., Breach, C.D., 1998. Thermodynamics of a stable blister delamination at elevated temperature. J. Adhes. 66 (1-4), 183–202.
- Wan, K.-T., Julien, S.E., 2009. Confined thin film delamination in the presence of intersurface forces with finite range and magnitude. J. Appl. Mech. 76, 051005 https://doi.org/10.1115/1.3112745.
- Wang, W., Gray, J.V., Julien, S.E., Wan, K.-T., 2018. Mechanical characterization of a convex shell (contact lens) with meridional thickness variation. Exp. Mech. 58 (6), 997–1002.
- Wong, M.-F., Duan, G., Wan, K.-T., 2007. Adhesion-delamination mechanics of a prestressed rectangular film adhered onto a rigid substrate. J. Appl. Phys. 101 (2), 024903. https://doi.org/10.1063/1.2422775.
- Zhu, T., Li, G., Müftü, S., Wan, K.-T., 2017. Revisiting the constrained blister test to measure thin film adhesion. J. Appl. Mech. 84 (7).